Supplemental material for:
"Multidimensional spectroscopy of nuclear spin clusters in diamond"

Konstantin Herb, Takuya F. Segawa, Laura A. Völker, John M. Abendroth, Erika Janitz,
Tianqi Zhu, and Christian L. Degen

I.   DIAMOND SAMPLES

All experiments were performed using a single-crystal diamond plate (Element6 Ltd.) of electronic grade with ^{13}C in natural abundance (1.1%). NV centers were created by ^{15}N$^+$ ion implantation at an energy of $5\,$keV with a dose of $4 \cdot 10^{10}\,$cm^{-2} (CuttingEdge Ions Ltd.). The sample was annealed at $850\,°$C to form NV centers. The sample was cleaned in a boiling 1:1:1 mixture of H$_2$SO$_4$:HNO$_3$:HClO$_4$ and baked at $465\,°$C in air. Nano-pillars were etched into the membrane surfaces to increase the photon collection efficiency (QZabre AG). The continuous wave (CW) photon count rate was $350-500\,$kcts/s. To remove organic contamination, the sample was cleaned in a 2:1 mixture of H$_2$SO$_4$:H$_2$O$_2$ before mounting in the setup.
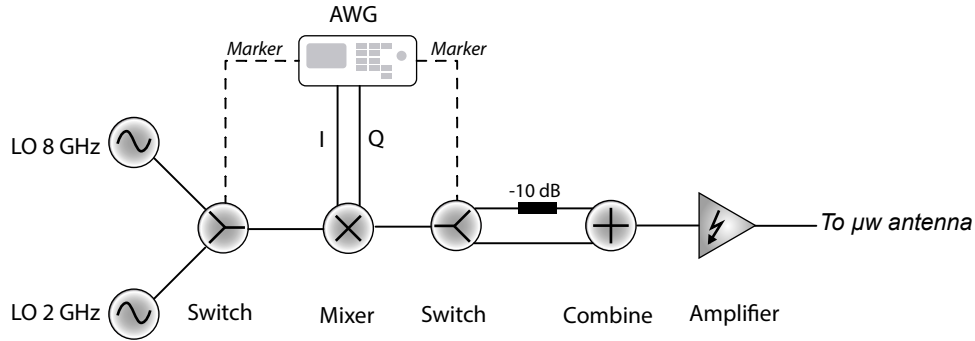
II.   INSTRUMENTATION

FIG. S1. Schematic diagram of the microwave system.

All experiments were performed using a custom-built confocal microscope equipped with a green $\lambda = 532\,$nm frequency-doubled Nd:YAG excitation laser (CNI Laser MSL-FN-532nm) and a $630-800\,$nm detection path using a single-photon avalanche photo diode (APD, PerkinElmer SPCM-AQRHfb Series). Optical pulses were generated by an acousto-optic modulator (AOM, Crystal Technology 3200-144) in a double-pass configuration, and gating of arriving photons was realized by time-tagging (NI-PCIe-6363) and software binning of photon counts. Typical laser excitation powers were on the order of $100\,\mu$W.

Microwave pulses for the manipulation of electronic spins were synthesized using an arbitrary waveform generator (AWG, Tektronix AWG5012C) and subsequent up-conversion. A schematic diagram of the full microwave path is shown in Figure S1. To create pulses at two separate frequencies, $\sim 2.5\,$GHz and $\sim 8.0\,$GHz, two local oscillators (Hittite HMC-T2100) were connected via an absorptive microwave switch (Analog Devices, HMC-C058) to one quadrature mixer (Marki

microwave IQ0218). Frequencies were selected for each individual pulse using a marker output of the AWG. A secondary switch at the mixer output allowed us to select a high-gain path and a low-gain path to mitigate resolution issues of the AWG output at low amplitude values. This is especially important for the Hartmann-Hahn condition that has to be fulfilled during the polarization phase of the experiment. The pulses were subsequently amplified using a broadband linear amplifier (Gigatronics GT-1000A). The microwave field at the NV center location origins from a coplanar waveguide (CPW) photo-lithographically defined on a quartz cover slip. The transmission line was terminated using an external $50\,\Omega$ load.

Switching speeds between the two LO frequencies were $< 4\,\mathrm{ns}$, allowing to perform inversions from the NV $m_s = +1$ state to $m_s = -1$ state in $< 100\,\mathrm{ns}$ (symmetric pulse lengths for both transitions $< 160\,\mathrm{ns}$). Here, we are mainly limited by the damping of the CPW at the frequency of the upper transition (8 GHz).

Radio-frequency (rf) pulses for nuclear spin manipulation were synthesized using an AWG (National Instruments PCI-5421) and subsequently amplified (Rohde & Schwarz BBA150). The rf pulses were applied using the system described in [1].

The bias field B_0 was aligned with the NV axis by adjusting the relative position of a cylindrical samarium-cobalt permanent magnet (TC-SmCo, reversible temperature coefficient 0.001%/K). The net magnetic bias field drifted typically by a few $\mu\mathrm{T}$, leading to variations in the EPR frequency of order $\pm 100\,\mathrm{kHz}$ and variations in the $^{13}\mathrm{C}$ Larmor frequency of $\pm 50\,\mathrm{Hz}$. This limited the observed $^{13}\mathrm{C}$ line widths. Magnetic field drifts were continuously tracked and logged by measuring the EPR resonance of the NV center, and the microwave excitation frequencies were periodically re-adjusted during the runtime of our experiment.

III. EXTENDED PULSE DIAGRAM

A. Polarization

Figure S2 provides a detailed overview of the pulse sequences used for the multidimensional spectroscopy. During the polarization phase, a ramped-amplitude NOVEL sequence is used to transfer spin polarization from the NV center to the nuclear spins. Since the NOVEL protocol requires the pre-polarization of the nitrogen spin of the NV center, the repeated application of the ramped NOVEL sequence is interspersed by a simple swap gate that flips the optically polarized NV spin state onto the nuclear spin of the ^{15}N . The spin-lock duration per repetition is typically $\sim 30 - 40\,\mu$s, and the NOVEL sequence is repeated ~ 1200 times. A nitrogen re-polarization is inserted after every fourth run of the NOVEL sequence.
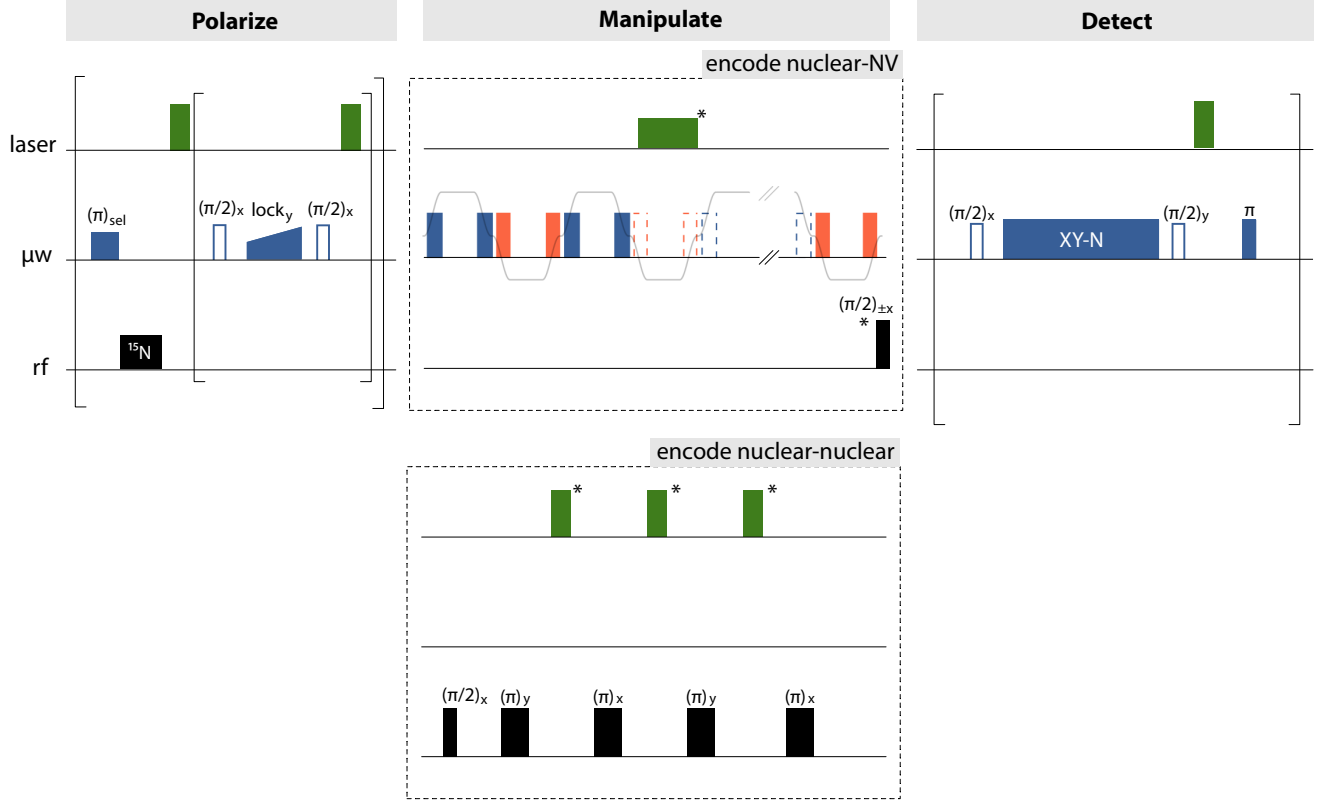

FIG. S2. Extended pulse diagram. The re-initialization laser pulses marked with an asterisk are optional. The $\pi/2$ marked with an asterisk can be left away if the azimuthal position is not of interest but only $a_\perp$ and $a_{||}$.

B. Manipulation

In the first experiment of the main text, we directly encode the hyperfine vector of a ^{13}C spin by periodically driving the NV center from $m_s = +1$ to $m_s = -1$ and back (upper segment in Fig. S2). An additional laser pulse can be used to reinitialize the NV center periodically. In order to continue to coherently drive the ^{13}C spins, it is crucial to "keep the clock" that periodically switches between $m_s = 1$ and $m_s = -1$. This would be analogous to simply muting the amplifier during re-initialization. By this, the nuclear spins continue to rotate after the laser re-initialization is completed and the time-periods can be treated as a periodic off-keying of the effective drive. This can then be accounted for in the analysis by re-scaling the measured $a_\perp$ values with the inverse of the duty cycle.

To encode nuclear-nuclear spin couplings, nuclear spin precession is induced by applying a resonant rf ($\pi/2$) pulse. Then, a train of refocusing π pulses follows as described in the main text. To reduce pulse-error accumulation, we perform a $XY4$ phase cycle. In case the NV coherence time is not long enough, the NV can also be periodically reinitialized. This is indicated by the laser pulses marked with an asterisk in Figure S2. Notably, the increment of the t_1 period has to be a multiple of the Larmor precession time to observe a symmetric spectrum centered around $\omega_1 = 0$. This is inherent to the NV center detection. While in conventional NMR, manipulation and detection happen in the same reference frame, this is not the case for weak-measurement type NV-NMR. If t_1 cannot be incremented accordingly (e.g., due to instrumentation limits), this can be corrected for in post processing by shifting along the ω_1 axis, i.e. multiplying the data with $e^{(-\mathrm{i}\Delta \cdot t_1)}$. If the correct Δ is unknown, it can be determined using a simple algorithm which assumes that most nuclear spins are not coupled: In a first step, the raw data is multiplied along the t_1 axis with $e^{(-\mathrm{i}\Delta \cdot t_1)}$, where Δ is guessed. Then, the mean with respect to both axes, t_1 and t_2, is subtracted in the time domain. Subsequently, the data is Fourier transformed. By summing over all entries of the power spectrum where $\omega_2 > 0$ we obtain the "moment" of the guessed offset Δ. The algorithm is repeated multiple times to minimize this norm by varying Δ.

C. Detection

The detection protocol is described in [2]. To get an encoding at $a_{||}/2$, we make sure that the NV center spends equal amounts of time in $m_s = 0$ and $m_s = -1$. For this, we insert a π pulse during the waiting time between the discrete sampling points of the weak-measurement acquisition.

4

IV. EFFECTIVE RABI FREQUENCY OBSERVED IN RABI SPECTROSCOPY

For the period length T, we can define the following waveform segment that describes the hyperfine field seen by the nuclear spin:

$$a_{\text{eff}}(t) = a_\perp \begin{cases} 0 & t < \frac{t_{\text{blk}}}{2} \\ \frac{1}{2} - \frac{1}{2}\cos\left(\pi \frac{t - t_{\text{blk}}/2}{t_\pi}\right) & \frac{t_{\text{blk}}}{2} < t < \frac{t_{\text{blk}}}{2} + t_\pi \\ 1 & \frac{t_{\text{blk}}}{2} + t_\pi < t < \frac{t_{\text{blk}}}{2} + t_\pi + t_{\text{plateau}} \\ \frac{1}{2}\cos\left(\pi \frac{t - t_{\text{blk}}/2 - t_\pi - t_{\text{plateau}}}{t_\pi}\right) + \frac{1}{2} & \frac{t_{\text{blk}}}{2} + t_\pi + t_{\text{plateau}} < t < \frac{t_{\text{blk}}}{2} + 2t_\pi + t_{\text{plateau}} \\ 0 & \frac{t_{\text{blk}}}{2} + 2t_\pi + t_{\text{plateau}} < t < \frac{3t_{\text{blk}}}{2} + 2t_\pi + t_{\text{plateau}} \\ \frac{1}{2}\cos\left(\pi \frac{t - 3t_{\text{blk}}/2 - 2t_\pi - t_{\text{plateau}}}{t_\pi}\right) - \frac{1}{2} & \frac{3t_{\text{blk}}}{2} + 2t_\pi + t_{\text{plateau}} < t < \frac{3t_{\text{blk}}}{2} + 3t_\pi + t_{\text{plateau}} \\ -1 & \frac{3t_{\text{blk}}}{2} + 3t_\pi + t_{\text{plateau}} < t < \frac{3t_{\text{blk}}}{2} + 3t_\pi + 2t_{\text{plateau}} \\ -\frac{1}{2} - \cos\left(\pi \frac{t - 3t_{\text{blk}}/2 - 3t_\pi - 2t_{\text{plateau}}}{t_\pi}\right) - \frac{1}{2} & \frac{3t_{\text{blk}}}{2} + 3t_\pi + 2t_{\text{plateau}} < t < \frac{3t_{\text{blk}}}{2} + 4t_\pi + 2t_{\text{plateau}} \\ 0 & \frac{3t_{\text{blk}}}{2} + 4t_\pi + 2t_{\text{plateau}} < t < 2t_{\text{blk}} + 4t_\pi + 2t_{\text{plateau}} \end{cases} \tag{1}$$

Calculating the Fourier series we find

$$a_{\text{eff}}(t) = a_\perp \sum_{n=0}^{\infty} \frac{2}{\pi} \frac{\left((-1)^n - 1\right) T^2 \left(\cos\frac{n\pi t_{\text{blk}}}{T} + \cos\frac{n\pi(t_{\text{blk}} + 2t_\pi)}{T}\right)}{8n^3 t_\pi^2 - 2nT^2} \sin\left(\frac{2\pi}{T}nt\right) \tag{2}$$

Most importantly, the first Fourier coefficient can be expanded up to the second order in t_{blk} and t_π to account for finite blanking periods and finite π pulses on the NV center transitions. We find

$$a_{\text{Rabi}} \approx a_\perp \frac{4}{\pi} \left(1 - \left(\pi^2 - 4\right)\frac{t_\pi^2}{T^2} - \frac{\pi^2}{2}\frac{t_{\text{blk}}^2}{T^2} - \pi^2 \frac{t_\pi t_{\text{blk}}}{T^2}\right) \approx a_\perp \frac{4}{\pi}\left(1 - \left(\pi^2 - 4\right)\frac{t_\pi^2}{T^2}\right) \tag{3}$$
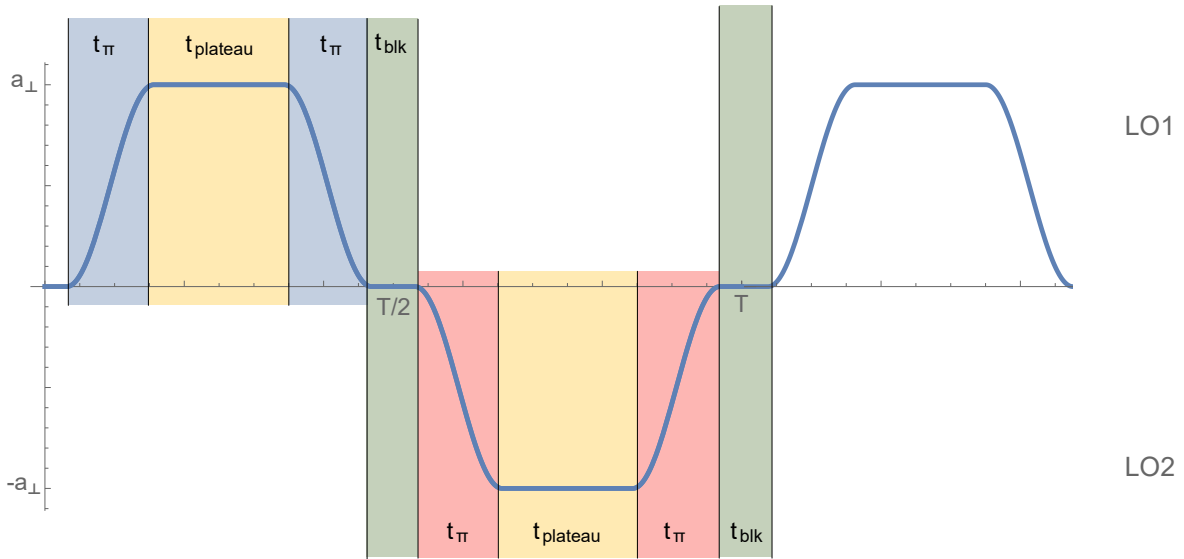

FIG. S3. Waveform segments of the waveform defined in (1).

This is in accordance with numerical simulations performed and can also be verified in a measurement.

Furthermore, a precise calibration of the pulse spacing (and therefore the drive frequency) is crucial as the expected Rabi frequency is rather small. However, by using a more strongly coupled nuclear spin, we can accurately determine the resonance frequency using correlation spectroscopy and tune the two-tone sequence itself by observing the generalized Rabi frequency behavior cf. Fig. S4.

(a)

$a_{\parallel} = 78$ kHz
$a_{\perp} = 168$ kHz
$f_0 = 1.9640$ MHz

(b) PSD (a.u.) vs Observed Rabi frequency (kHz)

Both transitions
Lower transition, slow pulses
Lower transition

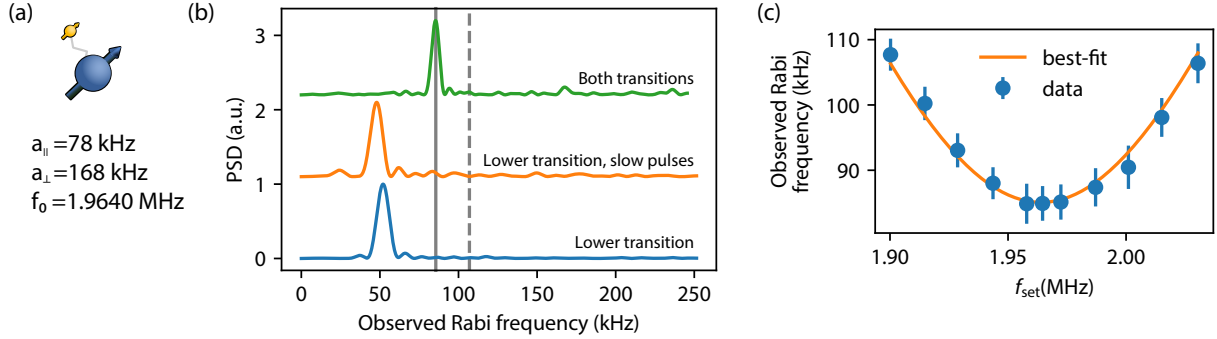(c) Observed Rabi frequency (kHz) vs f_{set}(MHz)

best-fit
data

FIG. S4. Rabi calibration for driving the nuclear spin via the hyperfine interaction. (a) System used for the calibration of the sequence. We use a relatively strongly coupled nuclear spin which we readout via state tomography. (b) Observed Rabi frequencies for situations using only one of the two NV transitions and the sequence introduced in the main text. The solid grey line indicates the expected Rabi frequency based on the hyperfine parameters for π pulses of 91 ns length. The hyperfine parameters were determined using correlations spectroscopy [3]. The grey dashed line shows the expected Rabi frequency for δ-like π pulses. (c) Observed generalized Rabi frequency when detuning the Rabi field.

V. ANALYTICAL TREATMENT OF NUCLEAR-NUCLEAR COUPLING SPECTROSCOPY

We start with a fully polarized spin system. Thus, the density operator for the product operator formalism calculation reads

$$\rho = I_{1,z} + I_{2,z} + I_{1,z} \cdot I_{2,z} \tag{4}$$

where $I_{i,j}$ are the spin operators for the ith spin ($i = 1, 2, .., j \in x, y, z$).
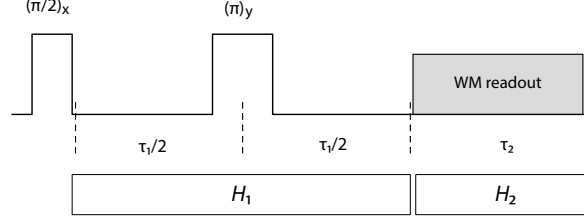
After the first $(\pi/2)_x$ pulse applied using the microcoil we have the product operator

$$\rho = -I_{1,y} - I_{2,y} + I_{1,y} \cdot I_{2,y} \tag{5}$$

During the indirect evolution period t_1 we evolve in the high-field approximation under the Hamiltonian

$$H_1 = \omega_0(I_{1,z} + I_{2,z}) + a \left[(I_{1,z} I_{2,z} - \frac{1}{4}(I_1^+ I_2^- + I_1^- I_2^+) \right] \tag{6}$$

with

$$a = \frac{\mu_0 \hbar}{4\pi} \frac{\gamma_C^2}{r^3} \left(1 - 3\cos^2\theta \right) \tag{7}$$

as the coupling constant. With a refocusing $(\pi)_y$ pulse interspersing two $\tau_1/2$ evolution periods, we obtain

$$\rho = -\cos\left(\frac{3a}{4}\tau_1\right)\left(I_{1,y} + I_{2,y}\right) + 2\sin\left(\frac{3a}{4}\tau_1\right)\left(I_{1,x} \cdot I_{2,z} + I_{1,z} \cdot I_{2,x}\right) + I_{1,y} \cdot I_{2,y} \tag{8}$$

where we can omit the last term as it does not lead to any observable coherence in the subsequent direct evolution time.

Next we let the system evolve for the time t_2. During this direct dimension, the evolution is governed by both, the coupling between the nuclei and by the imprint of the hyperfine coupling on the nuclear spins due to the weak measurement scheme. Therefore, the evolution is governed by

$$H_2 = \alpha I_{1,z} + \beta I_{2,z} + a \left[(I_{1,z} I_{2,z} - \frac{1}{4}(I_1^+ I_2^- + I_1^- I_2^+) \right] \tag{9}$$

where α and β denote the different precession frequencies due to the encoding of the parallel hyperfine coupling during the weak measurement readout.

We omit in the evolution all terms that do not lead to observable coherences, thus keeping only terms $\propto I_{i,x}$ and $\propto I_{i,y}$. For estimating the observed spectrum we can furthermore restrict ourselves w.l.o.g to the terms $\propto I_{i,y}$ and assume $\beta > \alpha$. Since the perpendicular couplings of nearby nuclear spins will be comparable, we can also sum the prefactors of the $\propto I_{1,y}$ and $\propto I_{2,y}$ and take this as our signal. We find

$$s(t) \propto \frac{a - \sqrt{a^2 + 4\Delta^2}}{2\sqrt{a^2 + 4\Delta^2}} \left[\cos\left(\frac{3}{4}at_1 + \left(-\frac{\alpha}{2} - \frac{\beta}{2} + \frac{a}{2} - \frac{\sqrt{a^2 + 4\Delta^2}}{4}\right)t_2\right) \right.$$
$$\left. + \cos\left(\frac{3}{4}at_1 + \left(\frac{\alpha}{2} + \frac{\beta}{2} + \frac{a}{2} - \frac{\sqrt{a^2 + 4\Delta^2}}{4}\right)t_2\right) \right]$$
$$-\frac{a + \sqrt{a^2 + 4\Delta^2}}{2\sqrt{a^2 + 4\Delta^2}} \left[\cos\left(\frac{3}{4}at_1 + \left(-\frac{\alpha}{2} - \frac{\beta}{2} + \frac{a}{2} + \frac{\sqrt{a^2 + 4\Delta^2}}{4}\right)t_2\right) \right.$$
$$\left. + \cos\left(\frac{3}{4}at_1 + \left(\frac{\alpha}{2} + \frac{\beta}{2} + \frac{a}{2} + \frac{\sqrt{a^2 + 4\Delta^2}}{4}\right)t_2\right) \right] \tag{10}$$

where $\Delta = \beta - \alpha$. Thus, we generally observe four peaks as the dipolar coupling between the nuclear spins splits the two peaks into four peaks in the direct dimension grouped into two pairs in the indirect dimension. It is insightful to take a look at two limits:

- $a = 0$: We observe two uncoupled nuclear spins, the observed signal

$$s(t) \propto \cos\left(\alpha t_2\right) + \cos\left(\beta t_2\right) \tag{11}$$

  is as expected: We see simply the superposition of two nuclear spin signal in the direct dimension. In the indirect dimension, we observe a constant signal (no separation on the vertical axis in the 2D Fourier transform).

- $a > \Delta$: The nuclear-nuclear dipole coupling is larger than the difference in the hyperfine coupling parameters of the two nuclei, the first term in (10) vanishes to the first order. This leaves us with only two peaks and explains why we see for nearest-neighbor coupling only two lines in the 1D spectrum,

$$s(t) \propto \cos\left(\frac{3}{4}at_1 + \left(\beta + \frac{3}{4}a\right)t_2\right) + \cos\left(-\frac{3}{4}at_1 + \left(\beta - \frac{3}{4}a\right)t_2\right) \tag{12}$$

  where we assumed $\alpha = \beta$. In the indirect dimension of the two-dimensional Fourier transform, the lines are $\frac{3}{4}a$ away from the horizontal zero line. One of the peaks is moved towards the positive frequency axis in the indirect dimension, the other towards the negative frequency axis.

Interestingly, an initial polarization imbalance between I_1 and I_2 leads to additional peaks which are caused by the flip-flop term of the dipolar interaction. However, we are assuming that they are greatly suppressed as adjacent nuclear spins should get the same initial polarization during the hyperpolarization phase of the experiment as their couplings to the NV center will be quite similar and additionally their local relaxation environment should be comparable. However, multi-spin effects can lead to an overall reduced polarization of both spins.

VI. LINEWIDTH LIMITATIONS

The observed linewidth is limited by a multitude of factors. In general, the effective transversal relaxation rate T_2 of the nuclear spins differs in the indirect and the direct dimension. In the direct dimension, the observed line-width can be broken down into four main contributions: The intrinsic decoherence of the nuclear spins Γ_{bare}, bias field drifts Γ_B, resiudal hyperfine coupling during optical illumination of the NV center Γ_γ and measurement-induced decoherence Γ_β.

- *Intrinsic decoherence* Γ_{bare}: The diamond lattice shields nuclear spins very well from the surrounding. However, paramagnetic defects, e.g., contribute to an intrinsic decoherence of the nuclear spins as well as finite dipolar coupling between $^{13}\mathrm{C}$ nuclei (and potential other spin-carrying nuclear spin impurities) causing a homogeneous broadening.

- *Bias field drift* Γ_B: Slow drifts in the spin-aligning bias field B_0 cause fluctuations in the Larmor frequency. Typically, our bias field is stable up to $\pm 5 \, \mu\mathrm{T}$. This translates to ~ 50 Hz variation of the $^{13}\mathrm{C}$ frequency.

- *Residual hyperfine coupling* Γ_γ: During readout, the perpendicular hyperfine interaction averages out due to Larmor precession, but the remaining parallel coupling leads to a random phase accumulation on the nuclear spin. This is due to the secular part of the hyperfine interaction. During optical illumination, the NV center cycles through its electronic states until it reaches a spin polarized steady state. This process involves stochastic jumps between spin states and possibly between electronic charge states. The transition rate for these jumps is proportional to the laser power. For typical coupling conditions, this translates to a broadening to ~ 10 Hz.

- *Measurement-induced decoherence* Γ_β: Inherently to the quantum mechanical measurement process, the nuclear spins are dephased with each readout block in the direct dimension. This causes a decay rate that is dictated by transverse component of the hyperfine interaction. In our measurements, this is typically the dominant contribution in the line-width. For the measurement conditions in the main text, this results in observed line-widths of ~ 250 Hz.

VII.   DATA CONSISTENCY FOR 2D HYPERFINE SPECTROSCOPY

The extracted hyperfine parameters and therefore positions of the 2D spectrum shown in Fig. 2 of the main text were verified with an additional consistency check. On NV A, a 1D weak-measurement trace with very much reduced sensitivity but an improved spectral separation of the features was taken. As described in [2], e.g., relative intensities and line-widths reduce with weaker and weaker measurements. Furthermore, the data was acquired with a different sampling interval. The Hamiltonian comprised of the Zeeman term and the dipolar hyperfine interaction was built using the positions inferred from the 2D spectrum. A simulation of the retaken 1D weak-measurement spectrum coincidences with the experimental data. Five nuclear spins can reproduce the majority of the spectral features present in this dataset.
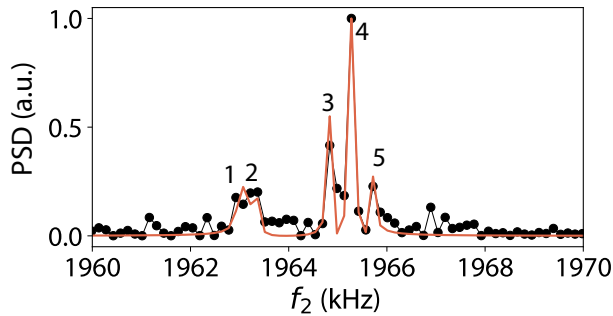

FIG. S5. Data consistency check: In (g), a simulation of a 1D weak-measurement spectrum of the reconnoitred 13C environment of (f) is captured with different measurement parameters (different measurement strength and different sampling). The orange curve coincidences with the measured 1D spectrum (black). Only 5 individual nuclear spins are sufficient to explain all major spectral features.

The values are tabulated below:

	$a_\parallel/2\pi$ (kHz)	$a_\perp/2\pi$ (kHz)	r (nm)	θ (°)	φ (°)
1	-2.4	13.9	1.23	59	-50
2	-1.8	13.8	1.24	58	0
3	1.7	16.4	1.21	51	70
4	2.6	36.3	0.92	53	10
5	3.4	12.0	1.35	46	-100

VIII.   POSSIBLE NUCLEAR-NUCLEAR SPIN COUPLINGS

Possible couplings present in the diamond host lattice are summarized in Table I. Figure S6 shows a histogram of the occurrence of the inter-nuclear couplings. Due to the r^{-3} dependence of the dipolar coupling, the large nuclear-nuclear spin couplings are especially sensitive to displacements in the lattice. We find that a variation of 0.1 A leads to a deviation of up to 700 Hz respectively 200 Hz for nearest neighbor couplings and up to 50 Hz for the next-nearest neighbor coupling.

d_{frac}	$d[\text{A}]$	N	θ	$f_1[\text{Hz}]$	d_{frac}	$d[\text{A}]$	N	θ	$f_1[\text{Hz}]$
0.433	1.544	1	0.0°	**-3094**	1.414	5.044	2	35.3°	-44
		3	109.5°	**1030**			5	90.0°	44
0.707	2.522	3	35.3°	**-355**			3	144.7°	-44
		6	90.0°	**355**	1.479	5.275	6	46.9°	-16
		3	144.7°	**-355**			6	73.0°	29
0.829	2.958	6	58.5°	40			5	95.6°	38
		3	100.0°	**200**			5	151.4°	-51
		3	150.5°	**-280**	1.581	5.640	6	43.1°	-19
1.000	3.567	2	54.7°	0			5	68.6°	19
		3	125.3°	0			5	111.4°	19
1.090	3.887	2	22.0°	-153			5	136.9°	-19
		6	97.6°	92	1.639	5.848	3	14.4°	-52
		3	131.5°	-31			3	95.0°	28
1.225	4.368	3	19.5°	-114			6	116.1°	12
		6	61.9°	23	1.732	6.178	1	0.0°	-48
		6	90.0°	68			3	70.5°	16
		6	118.1°	23			3	109.5°	16
		3	160.5°	-114			1	180.0°	-48
1.299	4.633	3	38.9°	-47					
		6	70.5°	38					
		6	123.8°	4					
		1	180.0°	-115					

TABLE I. Neighbors in the diamond lattice and corresponding coupling. Highlighted are couplings $\geq 200\,\text{Hz}$.
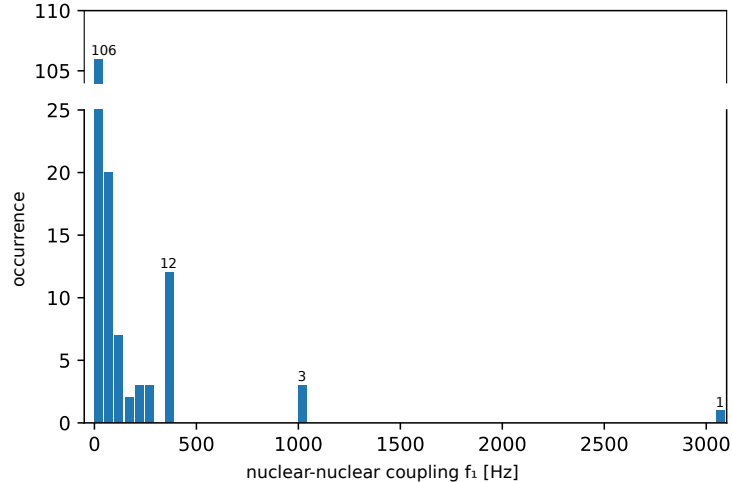
FIG. S6. Histogram of the occurence of nuclear-nuclear couplings in the diamond lattice. Bin width is 50 Hz. The probability to find a coupling $> 200\,\mathrm{Hz}$ is $\sim 20\%$.

IX. TRANSITION FROM WEAKLY TO STRONGLY COUPLED NUCLEAR SPIN PAIRS

To illustrate the change in number of observable peaks in the two-dimensional spectroscopy of spin pairs, we performed an explicit spin simulation. The results are shown in Fig. S7. For the simulation, we chose $a_{\parallel,1} = -2\pi \cdot 3\,\mathrm{kHz}$, $a_{\parallel,2} = 2\pi \cdot 3\,\mathrm{kHz}$ and $a_{\perp} = 2\pi \cdot 10\,\mathrm{kHz}$ for both spins. The bare Larmor frequency is 1967 kHz. We can clearly see the transition sketched in the main text: For essentially non-coupled spins, no displacement on the vertical axis is observed. In parallel to the splitting in the direct dimension (horizontal axis), we observe in total four peaks. The intensity of the four peaks is slightly differing resulting in potentially a reduced number of peaks depending on the choice of the contour levels for a given SNR. In the limit of nearly degenerate hyperfine couplings (as ω_{D} is much larger), we observe only two peaks. Note, that all 3 coupling regimes were observed experimentally: The uncoupled case is the trivial case, Fig. 3 shows for NV-C and NV-B the intermediate as well as the strong coupling regime, respectively.
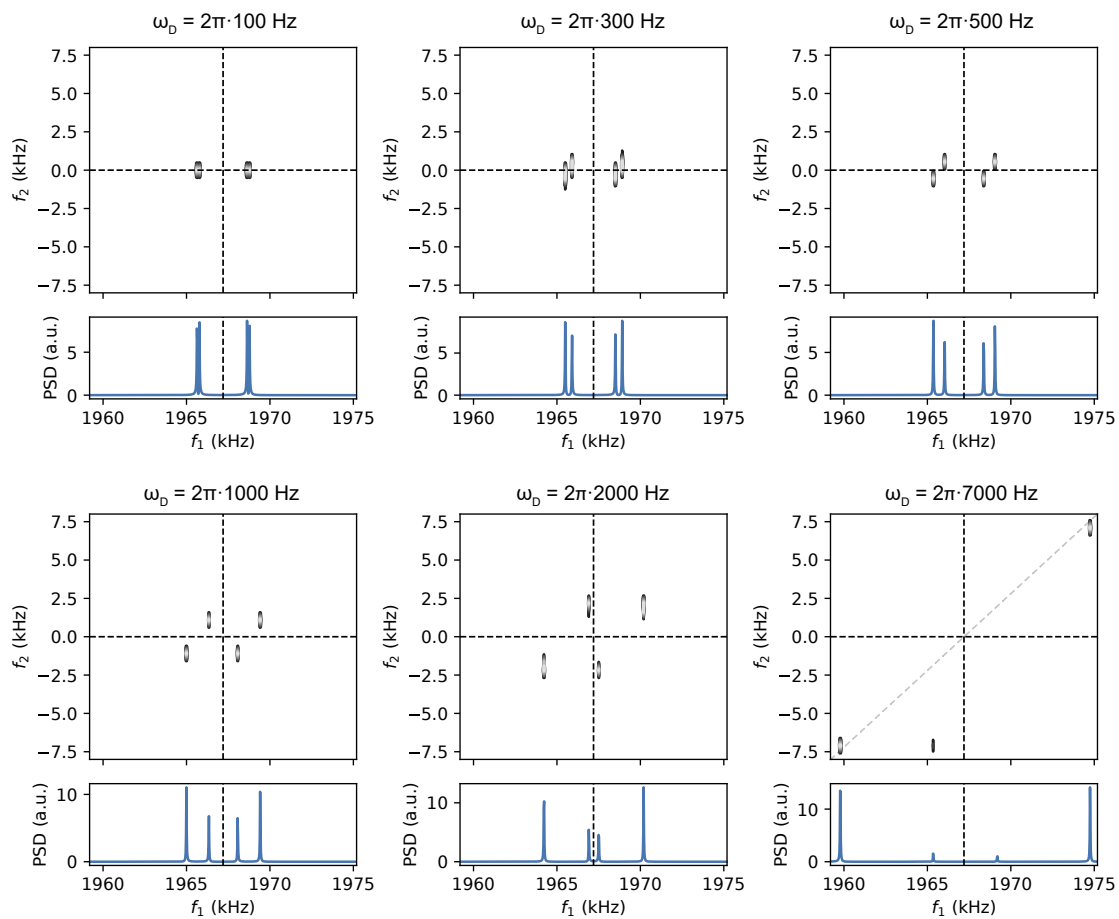
FIG. S7. Simulation of 2D spectra where we sweep the strength of the dipolar nuclear-nuclear coupling while keeping the hyperfine coupling to the NV center fixed.

13

X. DISJOINT CLUSTER SIMULATION

The experimental procedure was developed and verified using custom computer codes. For the typical sensitive volume around the NV center for the weak measurement protocol, it is impossible to perform a straight forward quantum mechanical simulation as the number of nuclei to consider is typically $\sim 10 - 20$. Therefore, a disjoint cluster approach was used. Here, nuclear spins lying within a certain threshold radius are grouped into spin clusters (typically, $10 - 20$ clusters were obtained using this procedure such that the system Hamiltonian dimensionality stays below $3 \cdot 2^6$). The simulation is then performed separately for each spin cluster and simulated weak-measurement traces are summed up afterwards.
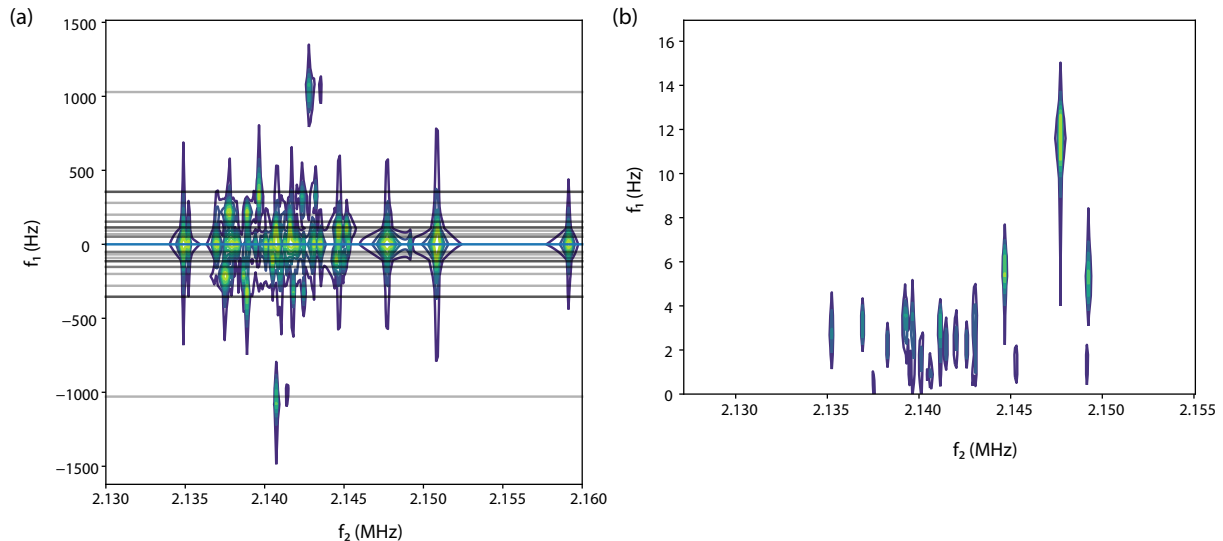

FIG. S8. (a) Two-dimensional spectrum encoding the nuclear-nuclear couplings. (b) Two-dimensional spectrum encoding the hyperfine parameters

[1] K. Herb, J. Zopes, K. S. Cujia, and C. L. Degen, **91**, 113106 (2020), URL https://doi.org/10.1063/5.0013776.

[2] K. S. Cujia, J. M. Boss, K. Herb, J. Zopes, and C. L. Degen, **571**, 230 (2019), URL https://doi.org/10.1038/s41586-019-1334-9.

[3] J. Boss, K. Chang, J. Armijo, K. Cujia, T. Rosskopf, J. Maze, and C. Degen, **116** (2016), URL https://doi.org/10.1103/physrevlett.116.197601.